OPEN ACCESS



B-fields and Dust in Interstellar Filaments Using Dust Polarization (BALLAD-POL). IV. Grain Alignment Mechanisms in the Cocoon Nebula (IC 5146) Using Polarization Observations from JCMT/POL-2

Saikhom Pravash^{1,2}, Thiem Hoang^{3,4}, Archana Soam¹, Eun Jung Chung^{3,5}, Diep Ngoc Pham^{6,7}, Nguyen Bich Ngoc^{6,7}, and Le Ngoc Tram⁸, Lindian Institute of Astrophysics, II Block, Koramangala, 560034, India; saikhom.singh@iiap.res.in, spravash11@gmail.com

Pondicherry University, R.V. Nagar, Kalapet, Puducherry, 605014, India

Korea Astronomy and Space Science Institute, 776 Daedeokdae-ro, Yuseong-gu, Daejeon 34055, Republic of Korea

University of Science and Technology, Korea, 217 Gajeong-ro, Yuseong-gu, Daejeon 34113, Republic of Korea

Department of Astronomy and Space Science, Chungnam National University, Daejeon, Republic of Korea

Department of Astrophysics, Vietnam National Space Center, Vietnam Academy of Science and Technology, 18 Hoang Quoc Viet, Hanoi, Vietnam
Graduate University of Science and Technology, Vietnam Academy of Science and Technology, 18 Hoang Quoc Viet, Hanoi, Vietnam

Leiden Observatory, Leiden University, PO Box 9513, 2300 RA Leiden, The Netherlands

Received 2025 February 15; revised 2025 July 4; accepted 2025 July 6; published 2025 August 22

Abstract

The polarization of starlight and thermal dust emission from aligned nonspherical grains provides a powerful tool for tracing magnetic field morphologies and strengths in the diffuse interstellar medium to star-forming regions, and constraining the properties of dust grains and their alignment mechanisms. However, the physics of grain alignment is not yet fully understood. The alignment based on radiative torques (RATs), known as RAT alignment or the RAT-A mechanism, is the most acceptable mechanism. In this work, we investigate the grain alignment mechanisms in the F13 (F13N and F13C) and F13S filamentary regions of the Cocoon Nebula (IC 5146) using observations of polarized thermal dust emission from James Clerk Maxwell Telescope/POL-2 at 850 μ m. We find that the polarization fraction decreases with increasing total intensity and gas column density in each region, termed a polarization hole. We investigate any role of magnetic field tangling in the observed polarization hole by estimating the polarization angle dispersion function. Our study finds that the polarization hole is not significantly influenced by magnetic field tangling, but is mainly due to the decrease in RAT alignment efficiency of grains in denser regions. To test whether the RAT-A mechanism can reproduce the observed results, we estimate the minimum alignment size of grains using RAT theory. Our study finds strong evidence for the RAT-A mechanism that can explain the polarization hole. We also find potential hints that the observed higher polarization fractions in some regions of the F13 filament can be due to the combined effects of both suprathermal rotation by RATs and enhanced magnetic relaxation, supporting the magnetically enhanced RAT mechanism.

Unified Astronomy Thesaurus concepts: Interstellar dust (836); Interstellar filaments (842); Star forming regions (1565); Interstellar magnetic fields (845)

1. Introduction

Dust grains in the interstellar medium, molecular clouds, and star-forming regions are very important elements that significantly influence various astrophysical processes such as star and planet formation, and gas heating and cooling, and they provide the surface on which to form gas molecules (see B. T. Draine 2003). J. S. Hall (1949) and W. A. Hiltner (1949) first observed the polarization of background starlight due to differential or selective or dichroic extinction by nonspherical grains aligned with the ambient interstellar magnetic fields. Since then, several studies have tried to explain the possible mechanisms for the alignment of the grains (e.g., L. J. Davis & J. L. Greenstein 1951; E. M. Purcell 1979; for a review see B. G. Andersson et al. 2015). However, these suggested mechanisms could not fully explain many observational results. The most acceptable mechanism of grain alignment that can explain various observational results in different environments from the diffuse interstellar medium and molecular

Original content from this work may be used under the terms of the Creative Commons Attribution 4.0 licence. Any further distribution of this work must maintain attribution to the author(s) and the title of the work, journal citation and DOI.

clouds to star-forming regions at different wavelengths from optical to submillimeter/millimeter is the alignment of grains based on radiative torques (RATs), known as the radiative torque alignment (RAT-A) mechanism. The RAT-A theory was first introduced by A. Z. Dolginov & I. G. Mitrofanov (1976) and numerically demonstrated by B. T. Draine & J. C. Weingartner (1997). An analytical RAT theory was later developed by A. Lazarian & T. Hoang (2007) and T. Hoang & A. Lazarian (2008). According to RAT-A theory, grains of nonspherical shape exposed to an external anisotropic radiation field experience radiative torques that tend to increase the spin of the grains far above the thermal rotation rate to suprathermal rotation and align the grains with the ambient magnetic field (B. T. Draine & J. C. Weingartner 1997; A. Lazarian & T. Hoang 2007). The grains achieve efficient alignment when they rotate suprathermally at a rotation rate greater than about three times their thermal angular velocity (T. Hoang & A. Lazarian 2008, 2016).

The aligned dust grains also re-emit polarized thermal emission at longer wavelengths (R. H. Hildebrand 1988). The dust polarization has been used widely to study the magnetic fields in various environments ranging from the diffuse interstellar medium to star-forming regions in molecular

clouds and also to study the properties of the dust grains such as shape, size, composition, etc. (e.g., B. T. Draine & B. S. Hensley 2021). Magnetic fields are thought to have significant influence on the formation and evolution of molecular clouds and to regulate the process of star formation (see R. M. Crutcher 2012; K. Pattle & L. Fissel 2019). The grains are aligned in such a way that their short axes are parallel and their long axes perpendicular to the ambient magnetic field (e.g., A. Lazarian 2007; B. G. Andersson et al. 2015; A. Lazarian et al. 2015). In the polarization of starlight due to dichroic extinction by aligned grains, the observed polarization angle traces the plane-of-sky (POS) projected magnetic fields. However, in the polarization of thermal dust emission, the observed polarization angle should be rotated by 90° to trace the POS-projected magnetic fields (e.g., R. H. Hildebrand 1988). Recent studies by T. Hoang & B. Truong (2024) and B. Truong & T. Hoang (2024) suggest the potential of tracing three-dimensional magnetic fields with full dust polarization data by comparing the observed dust polarization with an accurate model of dust polarization predicted from the grain alignment theory and dust properties. To study magnetic fields in the diffuse interstellar medium, molecular clouds, and star-forming regions more precisely using dust polarization as a reliable tool, it is important to study the exact physical mechanisms for the alignment of grains.

According to the RAT-A mechanism, there is expected to be an anticorrelation of the polarization fraction with the total emission intensity or the gas column density, and a correlation with the radiation field intensity or equivalently the dust temperature (see H. Lee et al. 2020; T. Hoang et al. 2021). A decreasing trend of the polarization fraction with increasing total emission intensity and gas column density, usually termed a polarization hole, is observed in various studies in different regions (e.g., K. Pattle & L. Fissel 2019; T. Hoang et al. 2021). The polarization hole may be caused by a decrease in grain alignment efficiency in denser regions as expected by RAT-A theory or by magnetic field fluctuations along the line of sight, or both. The main cause of magnetic field fluctuations is the turbulence in the molecular clouds (T. J. Jones 1989; T. J. Jones et al. 1992; D. Falceta-Gonçalves et al. 2008). Various studies in molecular clouds using starlight polarization support the RAT-A theory (for a review see B. G. Andersson et al. 2015). However, a test of the RAT-A mechanism in starforming regions using the observation of thermal dust polarization has only been conducted recently (see, e.g., L. N. Tram & T. Hoang 2022; N. B. Ngoc et al. 2023, 2024; S. Pravash et al. 2025) with the advancement in far-infrared and submillimeter/millimeter polarimetric instruments.

In this paper, we aim to study the grain alignment mechanism in the filamentary cloud regions of the Cocoon Nebula, a reflection nebula located in the eastern part of the star-forming molecular cloud IC 5146 in the constellation of Cygnus, using observations of thermal dust polarization from the James Clerk Maxwell Telescope (JCMT)/POL-2 at 850 μ m. This nebula consists of three filaments, namely F13, F13S, and F13W (E. J. Chung et al. 2021). Dense cores named C1, C2, C3, and C4 are identified in the F13 filament and dense cores C5, C6, and C7 in the F13S filament (E. J. Chung et al. 2024). These filaments and the core regions do not have bright embedded sources. A single B0V star BD +46°3474 (hereafter BD+46) is located at the center of

this nebula (in the southern part of F13 filament) (e.g., G. H. Herbig & B. Reipurth 2008; J. García-Rojas et al. 2014) surrounded by the H II region Sharpless 125 (S125; S. Sharpless 1959). The distance of the Cocoon Nebula is estimated to be 813 \pm 106 pc (J.-W. Wang et al. 2020) and that of BD+46 to be 800 ± 80 pc (J. García-Rojas et al. 2014). These filamentary regions of the nebula show significant variations in gas column density and dust temperature, or equivalently the radiation field strength across the filaments from the outer regions toward the inner regions. This makes them ideal regions for the study of the grain alignment mechanism in the context of RAT theory. In this work, we will study grain alignment only in the F13 and F13S filaments. The rest of the paper is organized as follows: Section 2 provides the details of observational data, Section 3 presents the data analysis and the results, Section 4 presents the discussions on the results, and Section 5 provides the conclusions.

2. Observations

2.1. Archival Polarization Data

In this work, we use the archival dust polarization data from E. J. Chung et al. (2024). The polarimetric observations were made with the POL-2 instrument (P. Friberg et al. 2016) on the JCMT at 850 μ m between 2021 June 9 and 2022 August 9 toward the F13 region of the Cocoon Nebula using the standard SCUBA-2/POL-2 daisy mapping mode, which covers a total observing area of diameter ≈11' with a central area of 3' diameter having the best sensitivity. The JCMT/ POL-2 instrument has FWHM of 14".1 at 850 μ m, which corresponds to ≈ 0.056 pc considering a distance of 813 pc to the Cocoon Nebula. For the reduction process, the data were reduced using the *pol2map* routine in the Sub-Millimeter User Reduction Facility (SMURF) package of the Starlink Software. For details of the polarimetric observations and the data reduction, please refer to Section 2.1 of E. J. Chung et al. (2024). In our analysis, we use debiased polarization data with the selection criteria $I/\delta I > 10$ and signal-to-noise ratio S/N > 2 ($P/\sigma_P > 2$) due to a limited and small sample of the polarization data. However, to see the validity of considering data points with 2 < S/N < 3, we check whether their inclusion affects the trends in our analyses as described in Section 3.1.2. In our analyses, we do weighted fitting in each analysis so that it will give more weight to the data with a higher signal-to-noise ratio.

2.2. H₂ Volume Density and Dust Temperature

In this work, we use the maps of H_2 column density $N(H_2)$ and dust temperature T_d of the Cocoon Nebula region of IC 5146 obtained from the Herschel Gould Belt Survey (P. André et al. 2010; D. Arzoumanian et al. 2011). The $N(H_2)$ map is the one given by E. J. Chung et al. (2024) with a resolution of 18″.2. The 18″.2 resolution of $N(H_2)$ is derived using the procedure described by P. Palmeirim et al. (2013). The dust temperature map has a resolution of 35″. The maps were obtained using Herschel PACS/SPIRE data at 70, 160, 250, 350, and 500 μ m. The maps are reprojected on the same grid as the JCMT 850 μ m intensity map and they have the same pixel scale of 4″ pixel⁻¹. For a particular pixel coordinate where polarization is detected, we create a circular region around this pixel coordinate in the $N(H_2)$ and T_d maps with a diameter of the JCMT beam size, 14″.1, and take the mean

Table 1
Properties of the Dense Cores Identified on the F13 and F13S Filaments Using the Same Procedure as Described by E. J. Chung et al. (2024)

Core ID	R.A. (J2000) (deg)	Decl. (J2000) (deg)	Size 1 (arcsec)	Size 2 (arcsec)	Effective Size (arcsec)	Size 1 (pc)	Size 2 (pc)	Effective Size (pc)
C1	328.403	47.317	9.66	8.6	9.12	0.04	0.03	0.04
C2	328.406	47.329	15.54	13.15	14.30	0.06	0.05	0.06
C3	328.396	47.348	22	18.35	20.09	0.09	0.07	0.08
C4	328.378	47.368	15.63	14.45	15.03	0.06	0.06	0.06
C5	328.442	47.293	13.53	8.31	10.61	0.05	0.03	0.04
C6	328.421	47.292	10.96	7.95	9.34	0.04	0.03	0.04
C7	328.398	47.291	16.41	10.95	13.40	0.06	0.04	0.05

Note. (i) Size 1 and Size 2 are the sizes of the major and minor axes and are deconvolved with the beam, i.e., size $= \sqrt{\text{size}_{\text{uncorrected}}^2 - \text{beam}^2}$ (D. S. Berry 2015). (ii) The effective sizes in both arcseconds and parsecs are the geometric means of Sizes 1 and 2, i.e., Effective Size $= \sqrt{\text{Size1} \times \text{Size2}}$. (iii) The physical sizes in parsecs are estimated considering a distance of 813 pc to the Cocoon Nebula.

value of all the pixel values found within this circular region. This mean value is used to compare with the JCMT/POL-2 data for that particular pixel coordinate.

We employ the column density map and estimate the H₂ volume densities for the F13 and F13S filaments separately, assuming a cylindrical geometry for each of them with different widths so that we can consider their depths or thicknesses to be equal to their diameters or widths. E. J. Chung et al. (2024) estimated the width of the F13 filament to be ≈ 0.32 pc and that of F13S to be ≈ 0.23 pc. However, we assume the embedded cores inside the filaments to have spherical geometries so that the sizes or diameters of the cores can be considered equal to the depths. The properties of the cores identified using the procedure described by E. J. Chung et al. (2024) with the FellWalker algorithm are given in Table 1. For the derivation of the gas volume density, we consider the F13 and F13S filaments as two separate cylinders with diameters 0.32 pc and 0.23 pc, respectively, and the embedded cores C1, C2, C3, C4, C5, C6, and C7 are assumed to have spherical geometries with effective angular diameters of 9.12, 14.30, 20.09, 15.03, 10.61, 9.34, and 13.40 that correspond to physical diameters of 0.04 pc, 0.06 pc, 0.08 pc, 0.06 pc, 0.04 pc, 0.04 pc, and 0.05 pc, respectively (see Table 1), considering a distance of 813 pc for the Cocoon Nebula. The volume densities are derived using the equation

$$n(\mathrm{H}_2) = \frac{N(\mathrm{H}_2)}{d},\tag{1}$$

where d is the depth of the filaments. We also note that the estimation of width or depth of filaments is biased based on the angular resolutions of the observations (G. V. Panopoulou et al. 2022). Also, our estimation of the volume density is based on the assumption of cylindrical geometries of these filaments and the spherical geometries of the embedded cores, which may not reflect the true three-dimensional structure of the filaments. The exact three-dimensional geometry of a star-forming filament is not yet fully known. However, a model assuming a cylindrical geometry of elongated filaments and a spherical geometry of the embedded cores stands to be a good approximation as found in various studies (e.g., P. C. Myers 2017; A. Kaminsky et al. 2023). Our study, which uses gas volume density values, is based on this assumption.

We combine the maps of $n(H_2)$ for both the F13 and F13S filaments into a single map, which is shown in Figure 1(left). The F13 filament has higher volume densities than the F13S

filament, with the highest values of more than $10^4 \,\mathrm{cm}^{-3}$ being found in the cores C1 and C2 in F13. For F13S, the core C7 has a high volume density of the order of $\approx 10^4$ cm⁻³. From the dust temperature map shown in Figure 1(right), we find that the core regions C1, C2, and C4 in F13 show a significant reduction in T_d values up to around 17 K. The F13 filament has a range of $T_{\rm d}$ values from 17.5 to 23 K and the F13S filament, which is less dense than F13, has a range of T_d values from 23 to 26 K. This F13S filament is near to the illuminating star BD +46, shown with a star symbol in the map. The higher $T_{\rm d}$ values in F13S can be due to its close proximity to BD+46 and being less dense. We find that the dust temperature decreases from the outside toward the inner regions of both the filaments. The dust temperatures in these filaments can be considered to be due to both the diffuse interstellar radiation field (ISRF) and the strong radiation from BD+46.

3. Analysis and Results

3.1. Data Analyses

3.1.1. Maps of Total Emission Intensity and Polarization Vectors

Figure 2 shows the map of the total emission intensity I of the filamentary regions of the Cocoon Nebula observed by JCMT/POL-2 at 850 μ m. The positions of the dense cores C1, C2, C3, and C4 in the F13 filament and C5, C6, and C7 in the F13S filament as identified by E. J. Chung et al. (2024) are circled in black in the figure. The small and the large dashed black circles denote the central region of 3' in diameter that has the best sensitivity and a total observing area of 11' in diameter, respectively. We use dashed black rectangles to mark two regions as F13N and F13C, which denote the North and the Center regions within the F13 filament, and a solid black rectangle to mark the F13S filament. Hereafter, we will use green for F13N, magenta for F13C, and black for F13S in all the analyses. We find that the regions of the cores C1 and C2 have higher intensities than other core regions.

We see that overall the core regions show higher intensity values than other regions. The intensity is found to be small in the outer regions of the filaments and it increases inwards.

Figure 3 shows the distribution of the polarization vectors overplotted on the total intensity map. The lengths of the vectors are proportional to the polarization fraction P and their orientations determine the magnetic field orientations. A reference scale length of P is indicated in the figure. We see that the value of P is large in the outer regions that have small

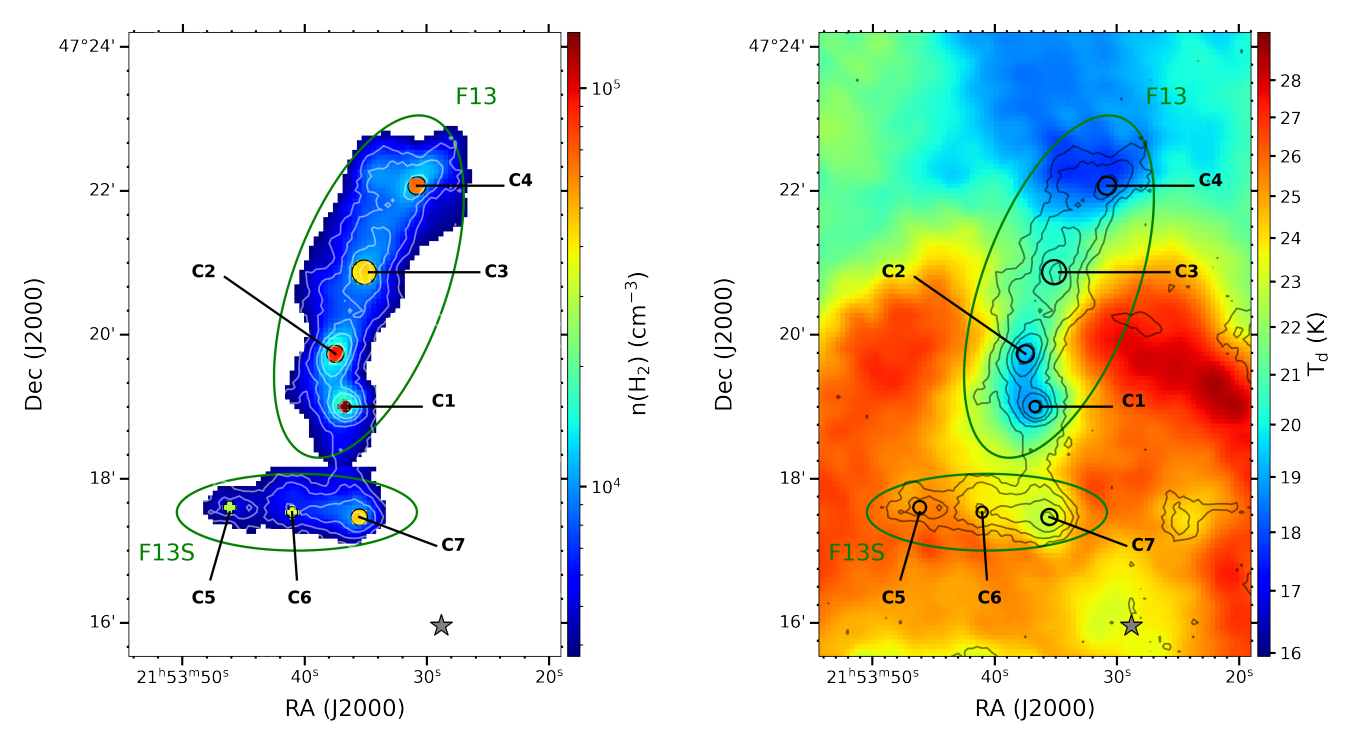


Figure 1. Maps of H_2 volume density (left) and dust temperature (right) for the F13 and F13S filaments of the Cocoon Nebula. The locations of the cores C1, C2, C3, and C4 in the F13 filament and C5, C6, and C7 in the F13S filament as identified by E. J. Chung et al. (2024) are indicated. The contours are drawn at total intensity *I* values of 12, 40, 80, 120, and 200 mJy beam⁻¹. The star symbol denotes the location of BD+46°3474 (BD+46).

intensities and decreases in the inner regions that are associated with higher intensities.

The left and right panels in Figure 4 show histograms of P for the F13N, F13C, F13S, and overall region of both the filaments for S/N > 2 and $S/N \ge 3$, respectively. The filled gray color is for all the regions. The median polarization fractions for the F13N, F13C, and F13S regions with S/N > 2are $5.67\% \pm 1.36\%$, $5.37\% \pm 2.38\%$, and $7.36\% \pm 3.43\%$, and for S/N > 3 they are 6.69% \pm 1.51%, 5.50% \pm 2.20%, and $9.19\% \pm 2.79\%$, respectively. The median polarization fractions for the combined regions with S/N > 2 and S/N > 3are $5.67\% \pm 2.48\%$ and $5.76\% \pm 2.31\%$, respectively. The two histograms show similar distributions of P, and the median values for S/N > 2 and S/N > 3 are nearly the same. The F13S filament is found to have higher P values than the F13 filament. This F13S filament is less dense than the F13 filament and located closer to the B-type star BD+46. The strong radiation from this star may increase the grain alignment efficiency in the outer regions of the F13S filament, producing a higher polarization fraction.

3.1.2. Variation of Polarization Fraction with Total Intensity, Gas Column Density, and Dust Temperature

In Figure 5, the variation of $T_{\rm d}$ with $N({\rm H_2})$ in each of the regions is shown. We see that the dust temperature decreases as the gas column density increases in each of the regions. This implies that denser regions are associated with lower dust temperatures or lower radiation field strengths due to the absence of bright embedded sources. The dust temperatures are due to the diffuse ISRF and the radiation from the BD+46 star only. In these denser regions, because of the weaker radiation field strength a large fraction of grains may not be able to achieve suprathermal rotation and can be randomized, according to the RAT alignment theory (T. Hoang et al. 2021),

after gas–grain collisions. This would result in the decrease of P in these denser regions. We analyze the variations of P with I, $N(H_2)$, and T_d in this section.

Figures 6(a) and (b) show the variations of the polarization fraction P with increasing total intensity I for S/N > 2 and $S/N \ge 3$, respectively. We see that P is very high, up to around 15% in the outer regions of both the filaments with I < 30mJy beam $^{-1}$, and it decreases with increasing I toward the filament's spine. The variations of P with I are fitted with power-law best-fit lines of the form $P = k_1 I^{a_1}$, where k_1 is a constant and a_1 is the slope of the fit. The best fits result in a_1 values of -0.71 ± 0.09 , -0.94 ± 0.04 , and -0.68 ± 0.05 for the F13N, F13C, and F13S filaments, respectively for S/N > 2, and -0.78 ± 0.09 , -1.06 ± 0.05 , and -0.67 ± 0.06 for $S/N \ge 3$. The data points shown as open circles are for 2 < S/N < 3. We find that the slope values of the weighted fits for both S/N > 2 and $S/N \ge 3$ are similar overall but they vary slightly for the F13C region. The inclusion of 2 < S/N < 3 data points does not significantly affect the trends observed when we exclude them.

Figures 6(c) and (d) show the variations of P with increasing gas column density $N(H_2)$ for S/N > 2 and $S/N \geqslant 3$, respectively. We find that P decreases with increasing $N(H_2)$ in each of the regions. Best power-law fits of the form $P = k_2[N(H_2)]^{a_2}$, where k_2 is a constant and a_2 is the slope, result in a_2 values of -1.61 ± 0.23 , -1.70 ± 0.07 , and -1.73 ± 0.14 for the F13N, F13C, and F13S filaments, respectively for S/N > 2, and -1.88 ± 0.25 , -1.67 ± 0.08 , and -1.79 ± 0.17 for $S/N \geqslant 3$. Here also, inclusion of data points with 2 < S/N < 3 does not significantly affect the observed trends. We see that P decreases with both increasing total intensity and increasing gas column density.

Figures 7(a) and (b) show the variations of P with increasing dust temperature T_d for each of the regions for S/N > 2 and

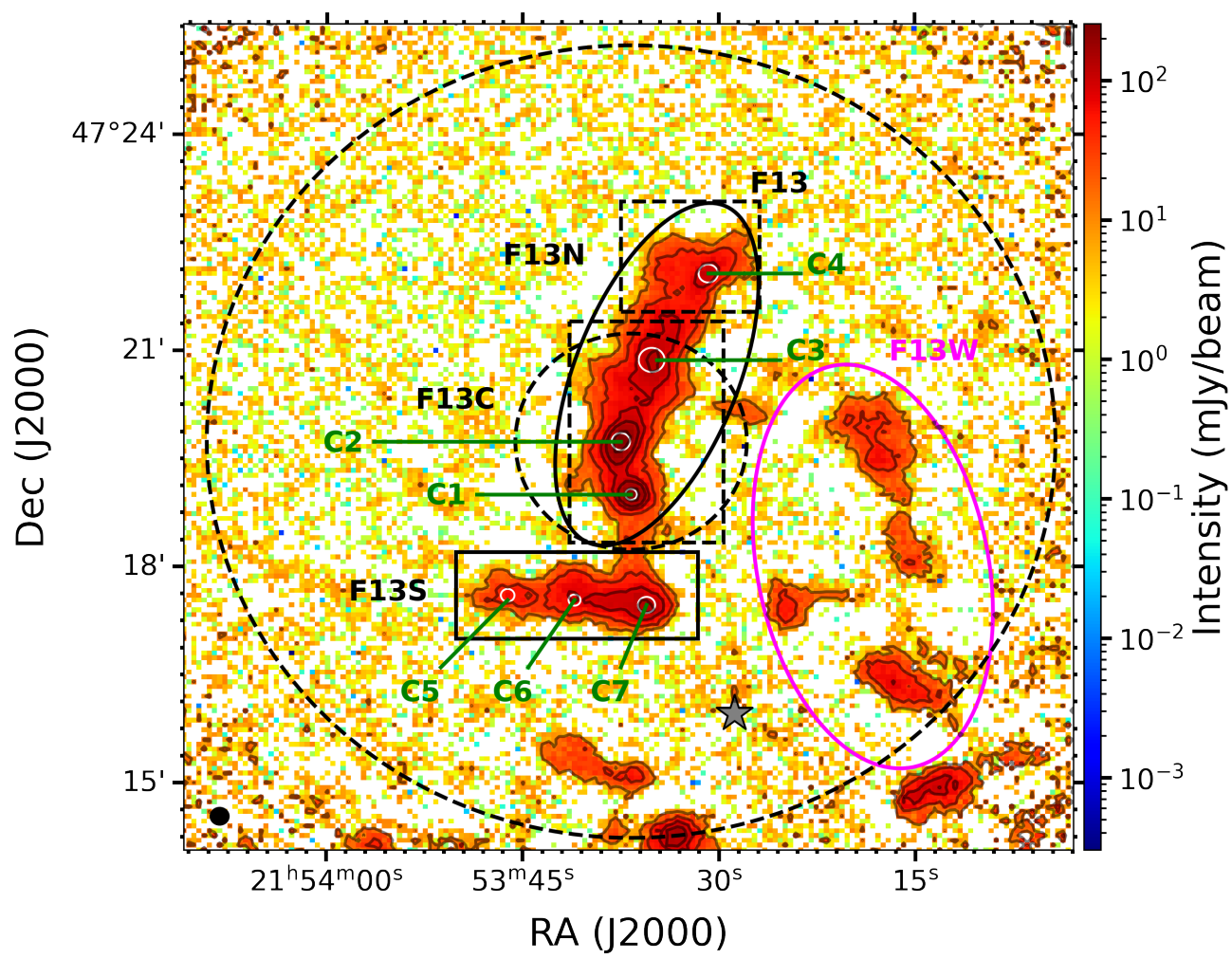


Figure 2. Map of total emission intensity (I) of the F13, F13S, and F13W filaments of the Cocoon Nebula observed by JCMT/POL-2 at 850 μ m with overlaid contours drawn at I values of 12, 40, 80, 120, and 200 mJy beam⁻¹. The positions of the dense cores C1, C2, C3, and C4 in the F13 filament and C5, C6, and C7 in the F13S filaments are indicated with white circles and labeled in green. The dashed small and large black circles are drawn at diameters of 3' and 11', and show the central area of best sensitivity and the total observing area, respectively. The solid black and magenta ellipses represent the regions of F13 that we study and F13W filaments, and the solid black rectangle represents the F13S filament region that we study. The F13 filament is further classified into two subregions shown as dashed black rectangles and named F13N and F13C, which denote the North and the Center regions of this filament. Also, the beam size, 14''. I, of JCMT/POL-2 at 850 μ m is indicated with a solid black circle at the lower left corner. The star symbol denotes the location of BD+46°3474 (BD+46).

 $S/N \geqslant 3$, respectively. P shows an overall increase with increasing T_d in the F13C and F13S regions. F13N shows some spread in the data; however, the weighted running mean shows a tendency to slightly increase in P with T_d for $S/N \geqslant 3$ and P shows a nearly flat distribution with T_d overall for S/N > 2 but we find some increase in P also. We see some data points that have smaller P values at larger T_d values, which may be due to tangling of the local magnetic field. Best power-law fits of the form $P = k_3 T_d^{a_3}$, with k_3 a constant and a_3 the slope, result in a_3 values of -1.37 ± 1.16 , 7.89 ± 0.37 , and 5.57 ± 0.86 for the F13N, F13C, and F13S regions, respectively for S/N > 2, and -1.31 ± 1.52 , 7.46 ± 0.38 , and 4.47 ± 0.96 for $S/N \geqslant 3$. The observed trends for both S/N > 2 and $S/N \geqslant 3$ are similar.

From our analysis of variations of P with I, $N(H_2)$, and T_d for both S/N > 2 and $S/N \geqslant 3$, because of the close similarity in the observed trends and also close similarity in the distributions of P (see Figure 4) for both of these signal-to-noise ratios, we consider data points with 2 < S/N < 3 in the subsequent analyses so as to increase the statistics of our

small data sample. However, we perform weighted analysis considering the uncertainties.

The decrease in P with I and $N(H_2)$ as seen in Figure 6 can be caused by the decrease in grain alignment efficiency in denser regions or magnetic field tangling, or both. We need to find out whether magnetic field tangling makes any significant contribution to causing the depolarization or not. For that, we analyze the effect of magnetic field tangling on the depolarization in the following section.

3.1.3. Polarization Angle Dispersion Function; Effect of Magnetic Field Tangling

The decrease in the polarization fraction with increasing total intensity and gas column density, widely known as a polarization hole, can be caused by the decrease in the alignment efficiency of the grains in the denser regions, as expected by RAT-A theory, or by fluctuations in the magnetic fields along the line of sight due to turbulence. To study whether the observed depolarization with increasing intensity and gas column density is due to the effect of magnetic field

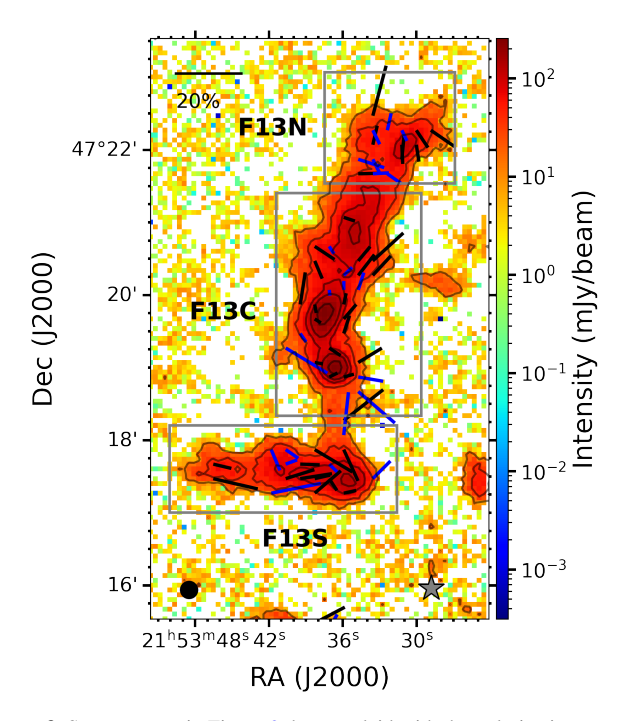


Figure 3. Same map as in Figure 2, but overlaid with the polarization vectors. The blue vectors are for $2 < P/\sigma_P < 3$ and the black vectors are for $P/\sigma_P \ge 3$. The lengths of the vectors are proportional to the polarization fraction P and their orientations determine the magnetic field orientations. A reference length scale of P of 20% is also indicated.

tangling along the line of sight or the decrease in grain alignment efficiency in the denser regions, or both, it is important to disentangle the effect of magnetic field tangling on the observed depolarization. We derive the polarization angle dispersion function denoted by S and calculate the product $P \times S$. The value of S provides an insight into the local nonuniformity in the distributions of the magnetic field morphology, and $P \times S$ provides information on the averaged grain alignment efficiency along the line of sight (Planck Collaboration et al. 2020). A higher value of S implies stronger magnetic field tangling, which can decrease the polarization fraction, and a lower S value implies weaker magnetic field tangling, which can result in a higher polarization fraction when considering a constant grain alignment efficiency along the line of sight.

To calculate *S*, we refer to the definition described in Section 3.3 of Planck Collaboration et al. (2020), which is given below

$$S^{2}(r, \delta) = \frac{1}{N} \sum_{i=1}^{N} [\psi(r + \delta_{i}) - \psi(r)]^{2},$$
 (2)

where the sum extends over N pixels, indexed by i and located at positions $r + \delta_i$, within a circle centered on r and having radius of δ , taken as twice the beam size of JCMT/POL-2. The term $[\psi(r + \delta_i) - \psi(r)]$ is the difference in the polarization angles at positions $r + \delta_i$ and r.

As the Stokes parameters Q and U are associated with noise, S becomes biased. This bias of S can be positive or negative depending on whether the true value is smaller or larger than the random polarization angle of 52° (D. Alina et al. 2016). An estimation of the variance of S ($S_{\rm db}$) resulting from noise along with the debiased values of S ($S_{\rm db}$) is described in Section 3.5 of Planck Collaboration et al. (2020) and they are given by the

following relations:

$$\sigma_S^2(r, \delta) = \frac{\sigma_\psi^2(r)}{N^2 S^2} \left[\sum_{i=1}^N \psi(r + \delta_i) - \psi(r) \right]^2 + \frac{1}{N^2 S^2} \sum_{i=1}^N \sigma_\psi^2(r + \delta_i) [\psi(r + \delta_i) - \psi(r)]^2$$
(3)

and

$$S_{\text{db}}^2(r,\,\delta) = S^2 - \sigma_S^2 \quad \text{if } S > \sigma_S. \tag{4}$$

We consider only those values of $S_{\rm db}$ with $S > \sigma_S$, discarding the other values that do not meet this criterion. Hereafter, we will refer to S as $S_{\rm db}(r,\delta)$ for convenience. Then, we examine how P varies with S as shown in Figure 8(a). Instead of using best-fit lines, we apply weighted running means for each region since the data points exhibit significant spread.

Best-fit lines do not adequately reflect the spread in the data, while the weighted running means provide a clearer representation of the variations. We see that there is not much significant correlation between P and S in each of the regions.

Then, we study the variations of the averaged alignment efficiency $P \times S$ with increasing I and $N(H_2)$ as shown in Figures 8(b) and (c). We find that $P \times S$ decreases with both increasing I and increasing $N(H_2)$, similar to the decrease in P with I and $N(H_2)$, which implies that the grain alignment efficiency decreases in the denser regions. Again, we study the variation of $P \times S$ with increasing T_d as shown in Figure 8(d) and find that $P \times S$ increases overall in a way more similar to the variation of P with T_d shown in Figure 7. The role of magnetic field tangling in causing the depolarization is found to be small and not very significant. Also, E. J. Chung et al. (2024) show that both the filaments are sub-Alfvénic, indicating the dominance of magnetic fields over turbulence.

3.2. Grain Alignment Mechanism

3.2.1. Minimum Alignment Size of Grains

The study of grain sizes is of great importance in the context of RAT-A theory to explain the grain alignment mechanism. According to RAT-A theory, efficient alignment of the grains can be achieved only when they rotate suprathermally at a rate exceeding about three times the thermal angular velocity (T. Hoang & A. Lazarian 2008, 2016). At this condition, the randomization of grains by gas–grain collisions can be ignored. The size distribution of aligned grains, spanning from the minimum alignment size, $a_{\rm align}$, to the maximum size, $a_{\rm max}$ (T. Hoang & A. Lazarian 2014; H. Lee et al. 2020), determines the polarization fraction. In order to get an insight into the variations in the polarization fractions in different regions of the filaments in the context of grain sizes, we estimate the values of $a_{\rm align}$ over all the filaments using the analytical relation given below as established by T. Hoang et al. (2021):

$$a_{\text{align}} \simeq 0.055 \hat{\rho}^{-1/7} \left(\frac{\gamma U}{0.1} \right)^{-2/7} \left(\frac{n_{\text{H}}}{10^3 \,\text{cm}^{-3}} \right)^{2/7} \times \left(\frac{T_{\text{gas}}}{10 \,\text{K}} \right)^{2/7} \left(\frac{\bar{\lambda}}{1.2 \,\mu\,\text{m}} \right)^{4/7} (1 + F_{\text{IR}})^{2/7}, \tag{5}$$

where $\hat{\rho} = \rho_{\rm d}/(3~{\rm g~cm}^{-3})$ with $\rho_{\rm d}$ being the dust mass density; γ is the degree of anisotropy of the radiation field; $\bar{\lambda}$ represents

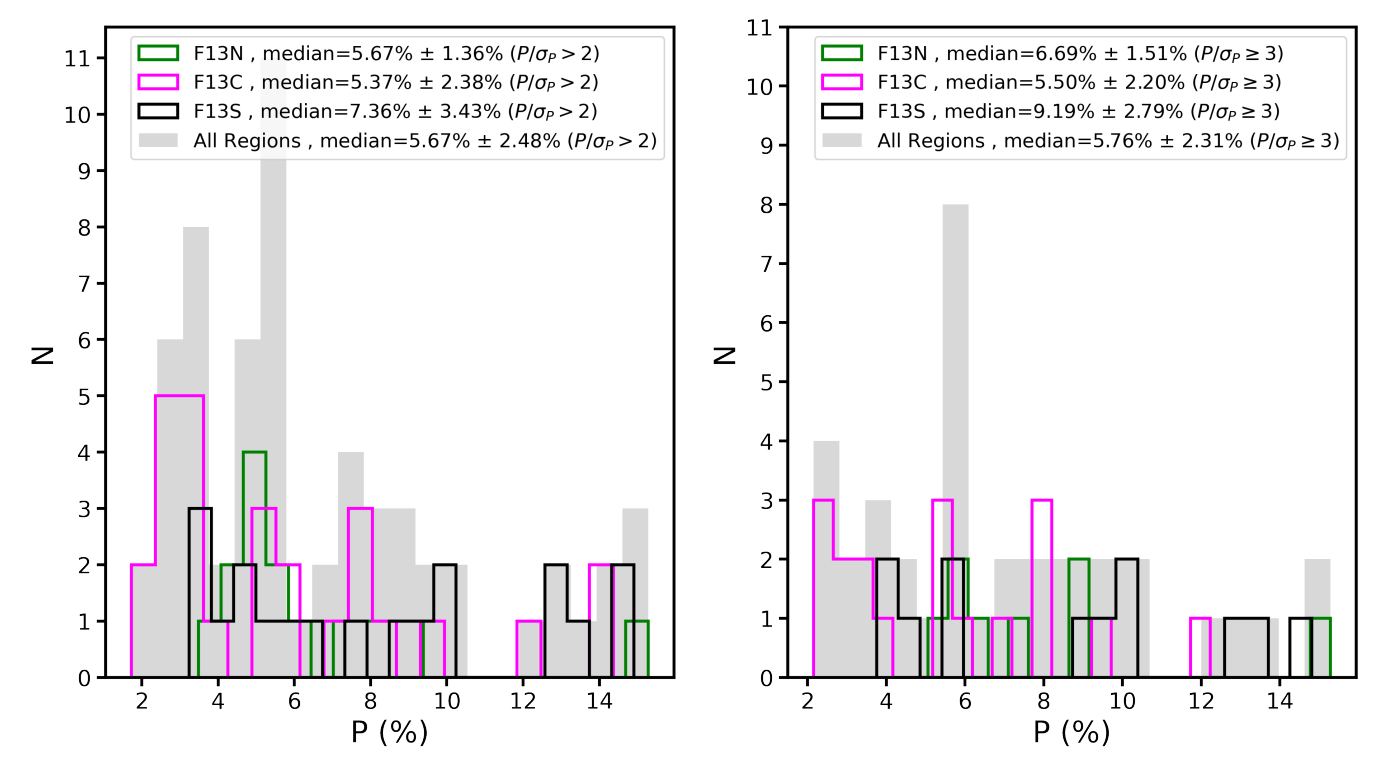


Figure 4. Histograms of the polarization fraction P for the F13N, F13C, and F13S regions and the combined regions of the F13 and F13S filaments for $P/\sigma_P > 2$ (left) and $P/\sigma_P \geqslant 3$ (right). The solid green, magenta, and black lines are for the F13N, F13C and F13S regions respectively. The filled gray color is for the combined regions of F13 and F13S filaments.

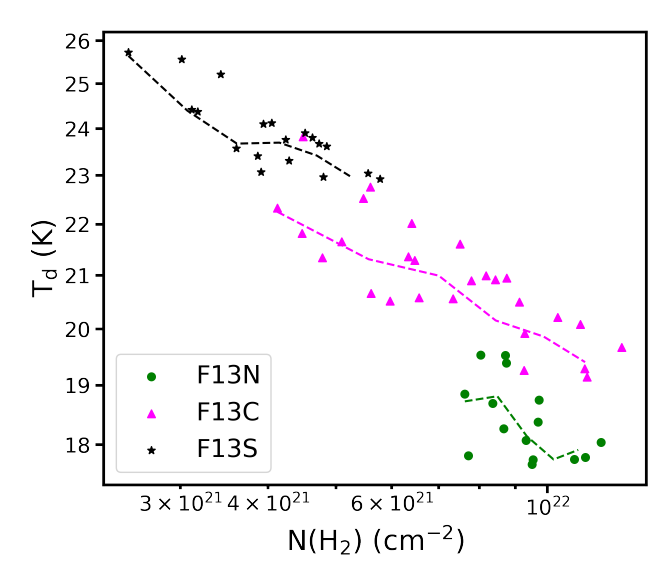


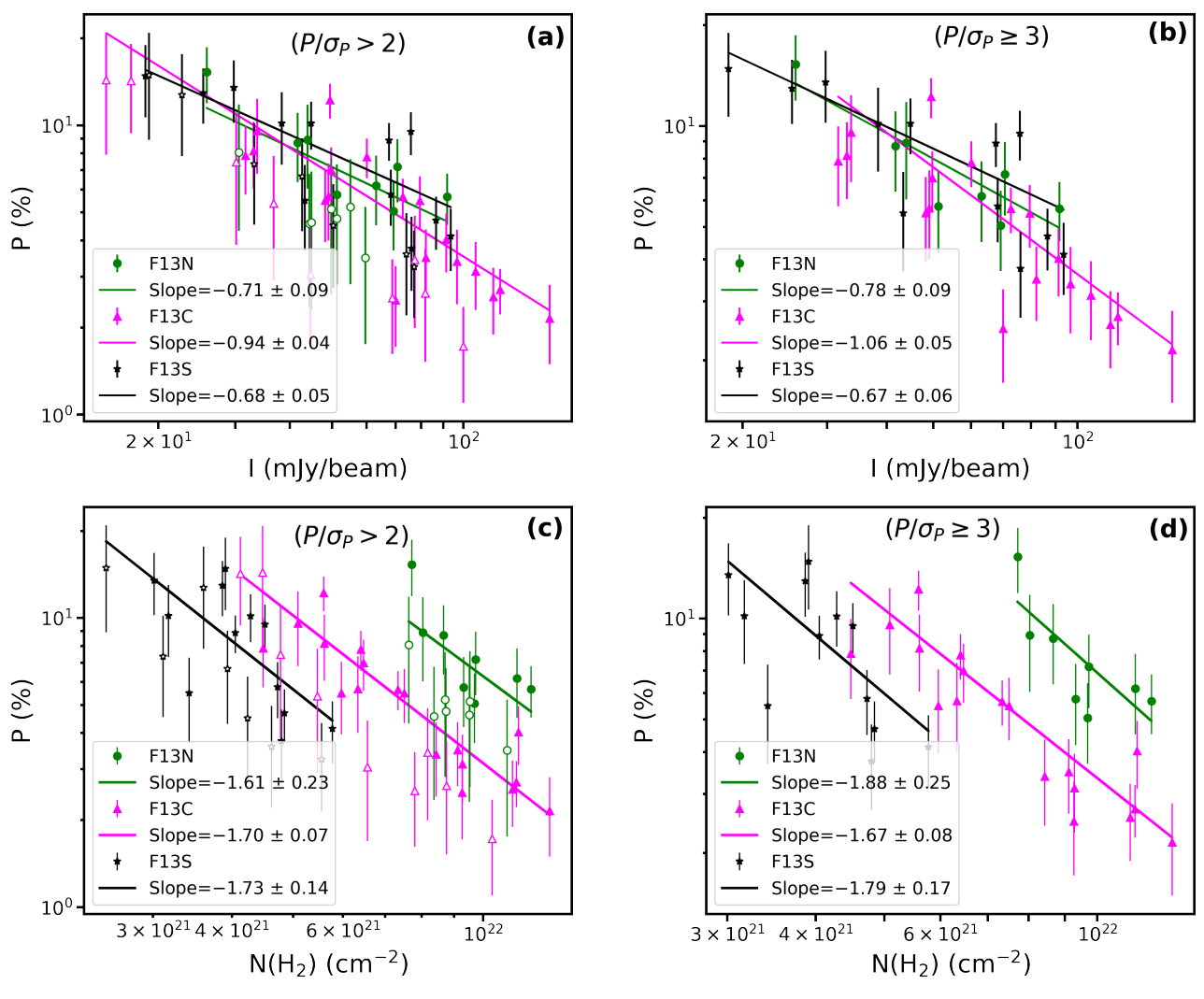
Figure 5. Variation of dust temperature with gas column density in each region.

the mean wavelength of the radiation; U is the radiation field strength; $n_{\rm H}$ is the number density of hydrogen atoms; $T_{\rm gas}$ is the gas temperature; and $F_{\rm IR}$ is the ratio of the IR damping to the collisional damping rate. For the diffuse ISRF, $\gamma=0.1$ (B. T. Draine & J. C. Weingartner 1997; T. J. Bethell et al. 2007). However, in our study we take $\gamma=0.3$ because the B-type star BD+46 is present nearby and hence the radiation becomes more anisotropic in the elongated dense filamentary clouds. We use $\rho_{\rm d}=3~{\rm g~cm}^{-3}, \bar{\lambda}=1.2~\mu{\rm m},$ and $n_{\rm H}=2n({\rm H_2})$ where $n({\rm H_2})$ is the volume density of molecular hydrogen gas

and $T_{\rm gas}=T_{\rm d}$ is considered because this thermal equilibrium between gas and dust is valid for dense and cold environments. For dense molecular clouds, $F_{\rm IR}\ll 1$.

To calculate U, we use the relation between dust temperature and the radiation strength for silicate grains having sizes in the range 0.01–1 μ m with dust heating and cooling balance and radiation strength $U < 10^4 \ (\approx 75 \ \text{K})$, i.e., $U \approx (T_d/16.4 \ \text{K})^6$ (B. T. Draine 2011). The map of the alignment size and the histogram distributions are shown in the left and right panels of Figure 9. The median values of a_{align} for the F13N, F13C, and F13S regions are found to be $0.09 \pm 0.01 \mu m$, $0.07 \pm 0.01 \mu m$, and 0.06 μ m and they are indicated in the figure with green, magenta, and black vertical dotted lines respectively. The histogram shows that the F13N and F13C regions have distributions of larger a_{align} values than the F13S region, which shows a distribution of smaller $a_{\rm align}$ values. Equation (5) shows that $a_{\rm align}$ varies with the radiation field strength U, or equivalently the dust temperature $T_{\rm d}$, as $U^{-2/7}$ and with the gas volume density $n_{\rm H}$ as $n_{\rm H}^{2/7}$. From the map of $a_{\rm align}$, we find that the F13N region shows a high value of a_{align} . This F13N region has high volume density and low dust temperature (see Figure 1). The densest core regions C1 and C2 in the F13C region show very high a_{align} values compared to other core regions. The F13S region is less dense and has higher dust temperature than other regions, and its a_{align} values are less. However, overall a_{align} increases from the outer regions toward the inner regions in both the filaments.

Within the framework of the RAT-A theory, the size of aligned grains ranges from $a_{\rm align}$ to $a_{\rm max}$, and the polarization fraction is determined by this range of grain size. The processes of grain growth and destruction determine the value of $a_{\rm max}$. When $a_{\rm max}$ is fixed, an increase in the value of $a_{\rm align}$



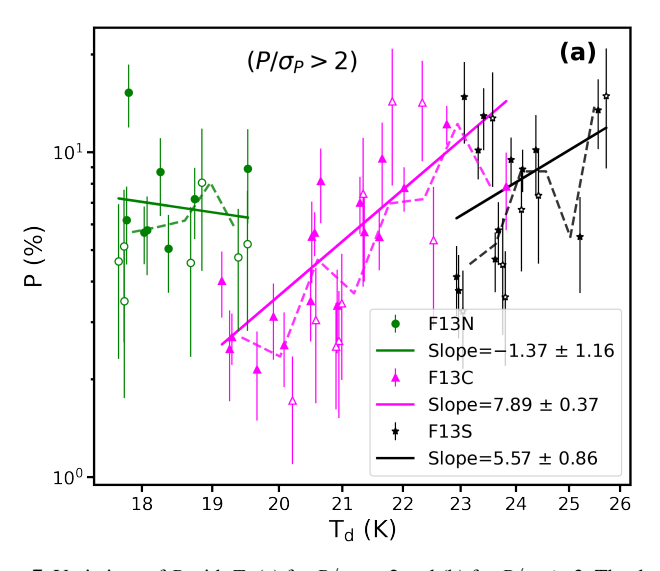
can provide a narrower size distribution of aligned grains, which can result in a reduction of the polarization fraction P. Again, a decrease in $a_{\rm align}$ can result in a wider size distribution of aligned grains, which can increase P (see Figure 7 n L. N. Tram & T. Hoang 2022). Therefore, an anticorrelation is expected between $a_{\rm align}$ and P. Also, we expect $a_{\rm align}$ to increase with the total intensity I in starless clouds.

Figure 10 shows the variation of $a_{\rm align}$ with I. We see that $a_{\rm align}$ linearly increases with I in each of the regions. Figure 11 shows the variation of P (left) and $P \times S$ (right) with $a_{\rm align}$. We plot weighted power-law fits and also weighted running means in each region. We see P decreases with increasing $a_{\rm align}$ in each of the regions and $P \times S$ also decreases with $a_{\rm align}$ in a similar manner, which implies that grain alignment efficiency decreases as $a_{\rm align}$ increases. Numerical modeling shows that polarization fraction decreases as $a_{\rm align}$ increases due to the reduction in the fraction of aligned grains (H. Lee et al. 2020; T. Hoang et al. 2021). The depolarization in each of the regions could be due to the decrease in the RAT alignment efficiency of grains in the denser regions of high column densities and low dust temperatures.

Table 2 summarizes the slope values of the weighted best power-law fits for each of the above different analyses.

3.3. Effect of Magnetic Relaxation on the RAT Alignment

In the investigation of grain alignment, the magnetic properties of dust are very important as these properties enable the grains to interact with the external magnetic field. When there is a diffuse distribution of iron atoms within a silicate grain, the grain behaves as an ordinary paramagnetic material. However, when iron atoms are distributed as clusters, the grain becomes superparamagnetic (T. Hoang et al. 2022). A paramagnetic grain that rotates with an angular velocity ω in the presence of an external magnetic field B undergoes paramagnetic relaxation (L. J. Davis & J. L. Greenstein 1951), which induces dissipation of the rotational energy of the grains into heat, resulting in the gradual alignment of angular velocity and angular momentum with B. This is known as the classical Davis-Greenstein mechanism and is applicable to any magnetic material. However, the efficient alignment of grains cannot be achieved by the paramagnetic relaxation alone due to randomization of grains by gas-grain collisions. Again, only RATs cannot produce perfect alignment of grains as the RAT alignment efficiency depends on various factors such as the angle between the directions of the radiation field and the magnetic field, and grain properties such as shape and composition (T. Hoang & A. Lazarian 2016; J. Herranen et al. 2021).



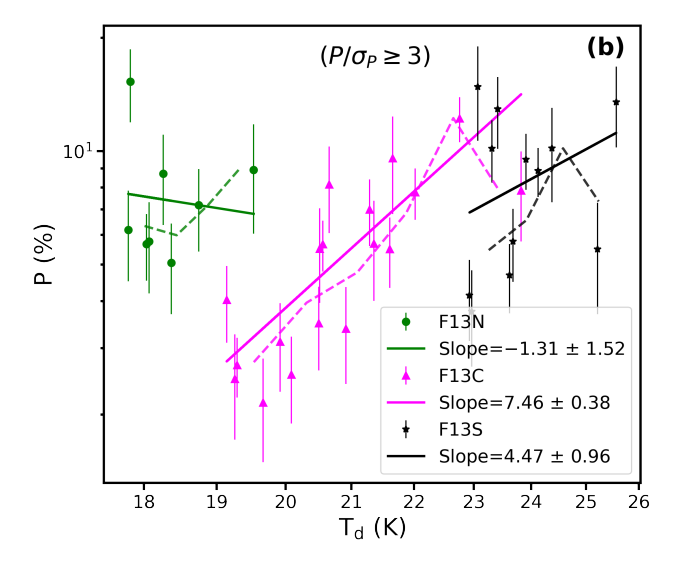


Figure 7. Variations of P with T_d (a) for $P/\sigma_P > 2$ and (b) for $P/\sigma_P > 3$. The data points shown as open circles are those associated with $2 < P/\sigma_P < 3$. The dashed lines are the weighted running means and the solid lines are the weighted best power-law fits.

In the filaments we study, it is observed that there are P values of more than 5%, reaching up to around 15%. Therefore, we explore the effect of magnetic relaxation on the RAT alignment efficiency by considering superparamagnetic grains that have embedded iron atoms as clusters, to explain the observed high P values, especially in the outer regions of the filaments. This consideration of the superparamagnetic nature of the grains is expected in denser regions due to the evolution of grains.

A dimensionless parameter δ_{mag} was introduced by T. Hoang & A. Lazarian (2016) to describe the aligning effect of magnetic relaxation relative to the disalignment caused by gas collisions. This parameter δ_{mag} provides the strength of the magnetic relaxation and is defined as the ratio of the gas collision damping timescale, τ_{gas} , to the magnetic relaxation time, $\tau_{mag,sp}$. For superparamagnetic grains that have embedded iron atoms as clusters, the strength of the magnetic relaxation is given by the following relation:

$$\delta_{\text{mag,sp}} = \frac{\tau_{\text{gas}}}{\tau_{\text{mag,sp}}}$$

$$= 56a_{-5}^{-1} \frac{N_{\text{cl}} \phi_{\text{sp,}-2} \hat{p}^2 B_3^2}{\hat{\rho} n_4 T_{\text{gas,}1}^{1/2}} \frac{k_{\text{sp}}(\Omega)}{T_{\text{d,}1}},$$
(6)

where $a_{-5}=a/(10^{-5}~{\rm cm}),~B_3=B_{\rm tot}/(10^3~\mu{\rm G}),~n_4=n_{\rm H}/(10^4~{\rm cm}^{-3})$ with $n_{\rm H}\approx 2n({\rm H_2})$ for molecular gas, $T_{\rm gas,1}=T_{\rm gas}/(10~{\rm K}),~T_{\rm d,1}=T_{\rm d}/(10~{\rm K}),~\hat{p}=p/5.5$ with $p\approx 5.5$ the coefficient describing the magnetic moment of an iron atom, $N_{\rm cl}$ gives the number of iron atoms per cluster, $\phi_{\rm sp}$ is the volume filling factor of iron clusters with $\phi_{\rm sp,-2}=\phi_{\rm sp}/0.01,$ and $k_{\rm sp}(\Omega)$ is a function of the grain rotation frequency Ω and is of order unity (T. Hoang et al. 2022).

When the magnetic relaxation occurs much faster than the gas collision damping, the magnetic relaxation strength is considered to be effective for the alignment of grains. The degree of RAT alignment of grains can be significantly enhanced by the combined effect of both the suprathermal rotation of grains by RATs and the strong magnetic relaxation, which is termed the magnetically enhanced radiative torque (M-RAT) mechanism of grain alignment.

To calculate the magnetic relaxation strength $\delta_{mag,sp}$ in all regions of the F13 and F13S filaments using Equation (6), we use the pixel values of the plane-of-sky magnetic field strength B_{POS} from the B_{POS} pixel-by-pixel map as given in Figure 16 (left) of E. J. Chung et al. (2024). For details of the estimation of the B_{POS} map, please refer to Figures 12, 15, and 16 of E. J. Chung et al. (2024). In this map, B_{POS} values are estimated only for 24 pixels over the F13 and F13S filaments, and lacks information for the other pixels. Therefore, our calculation of $\delta_{\text{mag,sp}}$ will be limited to only these 24 pixels, having B_{POS} information. We calculate the total magnetic field strength B_{tot} by multiplying B_{POS} by a factor of 1.3 (R. M. Crutcher et al. 2004). We use $N_{cl} = 100$ and $\phi_{\rm sp}=0.01$ (about 3% of iron abundance as iron clusters, T. Hoang & A. Lazarian 2016). We calculate the $\delta_{\text{mag,sp}}$ values for those 24 pixels using the values of all the parameters in Equation (6). The map of the strength of magnetic relaxation is shown in the left panel of Figure 12. The relation between the polarization fraction P and $\delta_{\rm mag,sp}$ for each region, with the colors denoting the a_{align} values, is shown in the right panel of Figure 12. The values of $\delta_{mag,sp}$ in the F13N region are in the range from 6 to 53 with a median value of around 18; those in the F13C region are in the range from 13 to 667 with a median value of around 28, and those in the F13S region are from 2 to 6 with a median value of around 2. We find some pixels associated with high B_{POS} values in the F13C region and having high magnetic relaxation strength $\delta_{\text{mag,sp}} \gg 10$. The P values in the corresponding pixels are also found to be high, ranging from around 5% to 8%. We expect that there may not be strict correlation between P and $\delta_{\text{mag,sp}}$ as the pixels are associated with different a_{align} values and P also depends on $a_{\rm align}$ values. In F13C, we see the increase in P as $\delta_{\rm mag,sp}$ increases and a_{align} decreases in Figure 12. The F13N region also has $\delta_{\rm mag,sp}$ > 10 in some pixels, with high P values ranging from 5% to 8%. However, we see some fluctuations in P values in the F13N region. The F13S region has small B_{POS} values overall and $\delta_{\rm mag,sp} \ll 10$ (for a discussion see Section 4.2). More observational data are needed to better understand the role of enhanced magnetic relaxation in the RAT alignment or the M-RAT mechanism in these filaments.

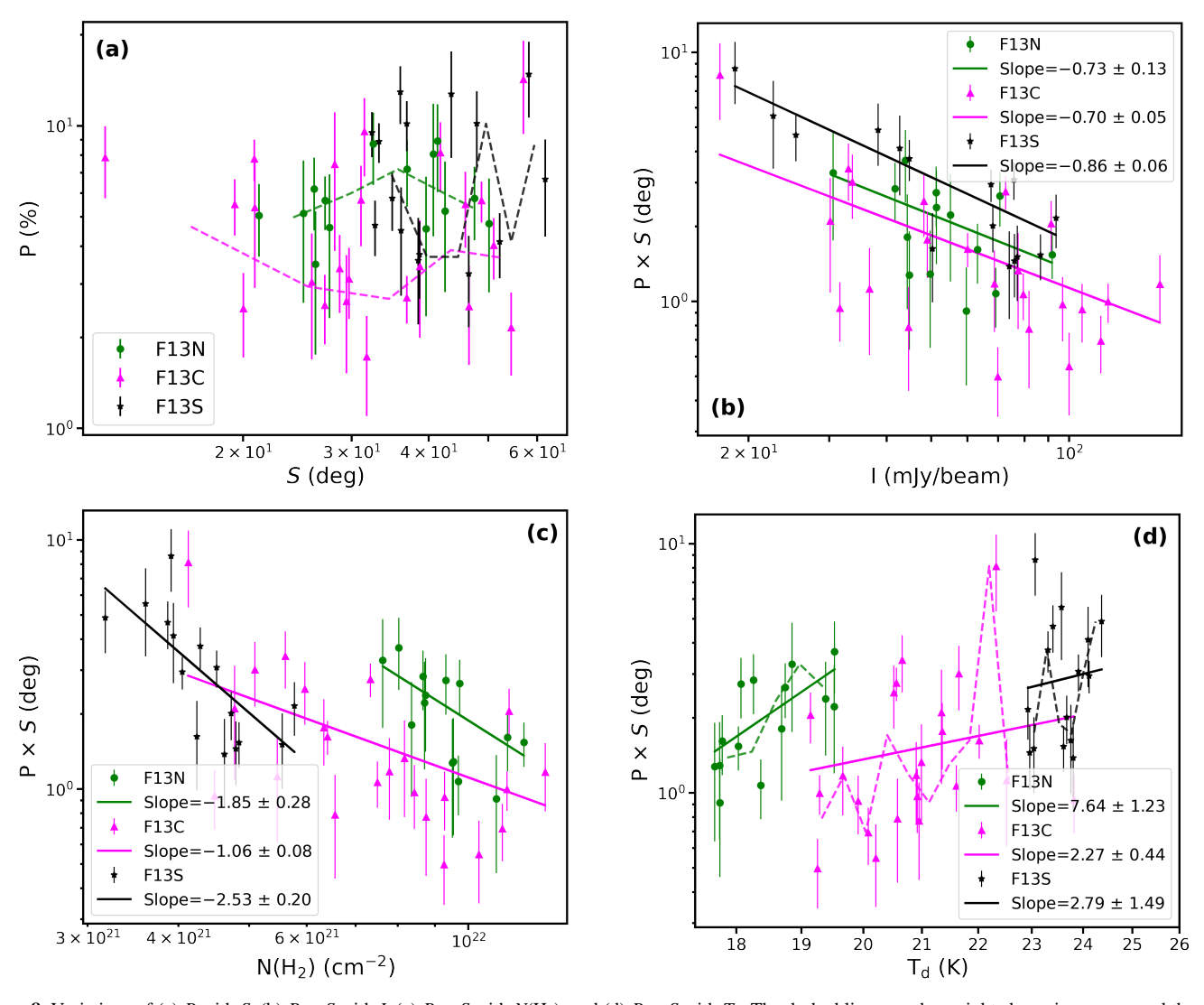


Figure 8. Variations of (a) P with S, (b) $P \times S$ with I, (c) $P \times S$ with $N(H_2)$, and (d) $P \times S$ with T_d . The dashed lines are the weighted running means and the solid lines are the weighted best power-law fits.

4. Discussions

In this section, we will discuss our results to explain the mechanism of grain alignment in each of the regions of the filaments.

4.1. Evidence for the Alignment of Grains by the RAT-A Mechanism

4.1.1. Decrease in the Polarization Fraction with the Total Intensity and Gas Column Density

Observational studies of dust polarization in various environments from the diffuse interstellar medium to molecular clouds, filaments, and star-forming regions reveal that the polarization fraction decreases with increasing total intensity and gas column density, which is widely known as a polarization hole (see, e.g., K. Pattle & L. Fissel 2019; T. Hoang et al. 2021). However, the exact cause of the polarization hole is still not clear. The significant decrease in the grain alignment in the denser regions that have no embedded sources, caused by weaker RATs for uniform magnetic fields, acts as the leading explanation for the polarization hole (T. Hoang et al. 2021). The polarization hole can also be

caused by fluctuations in the magnetic field orientations along the line of sight. These fluctuations in the magnetic fields are suggested to be due to turbulence in the region (T. J. Jones 1989; T. J. Jones et al. 1992; D. Falceta-Gonçalves et al. 2008).

The F13 and F13S filaments do not contain prominent bright embedded sources. However, there is a single B-type star, BD+46, in the Southern part of F13 filament. This environmental feature makes this region favorable for the study of the grain alignment mechanism in the context of RAT theory. The diffuse ISRF and the radiation field from the nearby star BD+46 act as the main radiation sources for grain heating and alignment in these regions.

In the P–I and P– $N(H_2)$ plots (see Figure 6), the polarization fraction is found to decrease with increasing total intensity and gas column density. Again, in the T_d – $N(H_2)$ plot (see Figure 5), the dust temperature decreases with increasing gas column density, which implies the absence of bright embedded sources. The only source of grain heating is from the nearby star BD+46 and the diffuse ISRF, and the external radiation field strength decreases in the denser regions. Since the F13 and F13S filaments lack bright embedded sources, the high gas density in the denser regions dominates over the weak

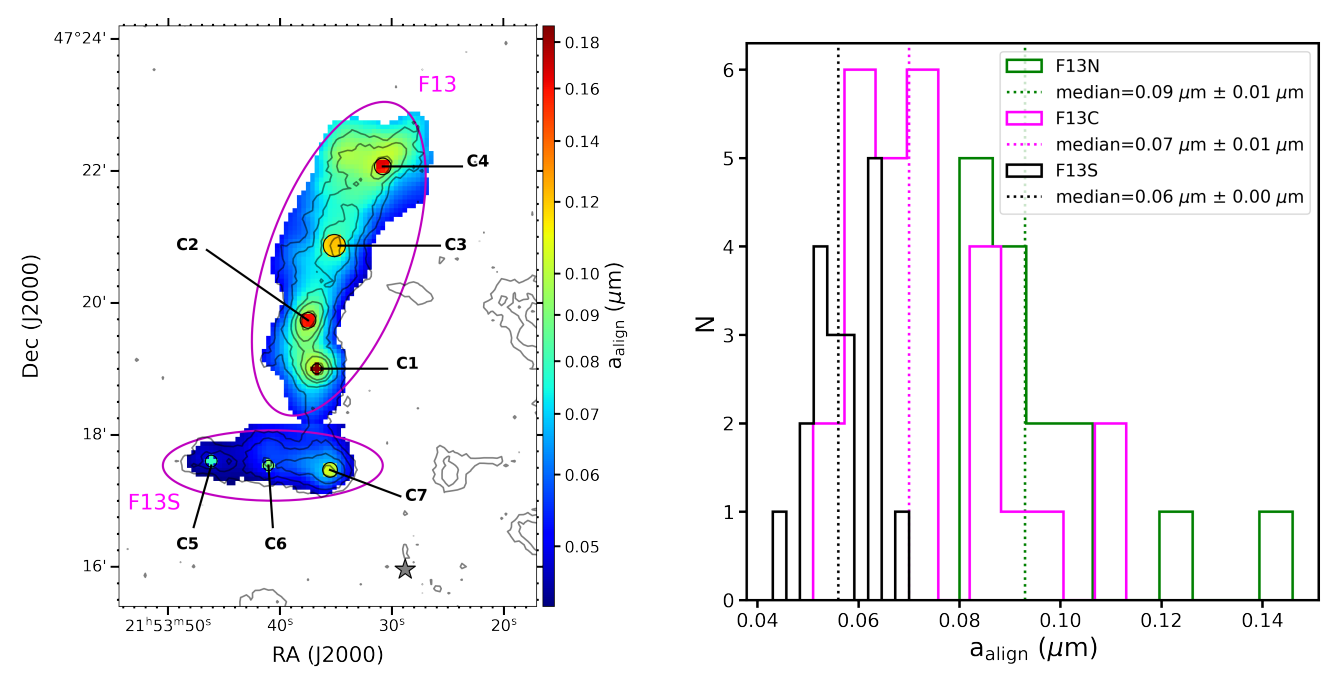


Figure 9. Map of the minimum alignment size of grains, a_{align} (left), and the histograms of a_{align} in each of the F13N, F13C, and F13S regions (right). The vertical dotted green, magenta, and black lines denote the median values of a_{align} in F13N, F13C, and F13S regions, respectively.

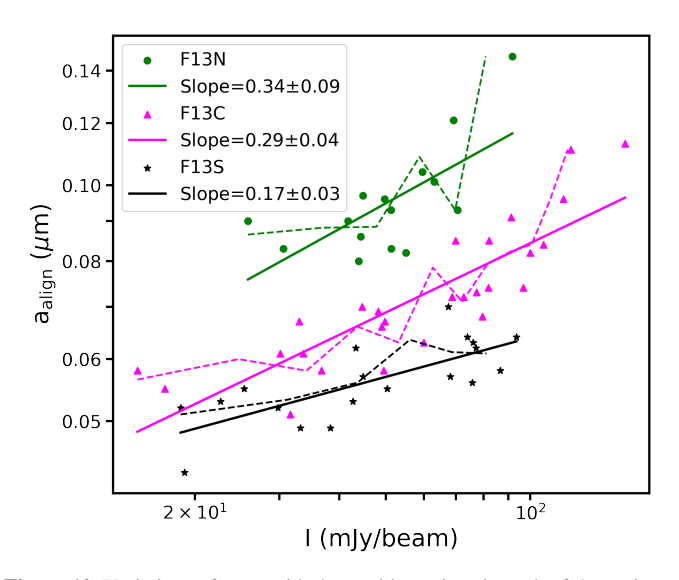


Figure 10. Variations of a_{align} with the total intensity I in each of the regions. The dashed lines are the running means and the solid lines are the best power-law fits.

radiation and randomizes the grains due to gas-grain collisions, resulting in the decrease in grain alignment efficiency in these denser regions. We see high values of polarization fraction in the outer regions of the filaments, up to around 15%. This may be due to the efficient alignment of grains in these outer regions by the strong radiation field from the BD+46 star. However, this radiation will get attenuated significantly as it traverses through the denser regions.

We also show that the magnetic field tangling does not have a significant effect on the observed depolarization from our analyses of the variations of P with S, and $P \times S$ with I, $N(H_2)$, and T_d (see Figure 8). Hence, the depolarization in the denser regions is mainly due to the decrease in the alignment efficiency of grains in the denser regions, in agreement with

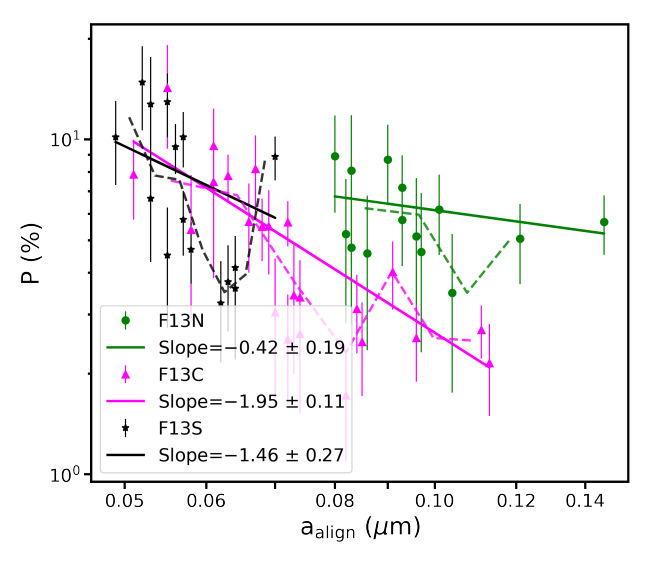
the RAT theory. The similar observed feature that the depolarization in the denser regions is predominantly due to a significant decrease in grain alignment efficiency, with the *B*-field tangling playing a subdominant and less significant role, was also found in the study of dense and cold filaments that do not have prominent embedded bright sources—G11.11-0.12 by N. B. Ngoc et al. (2023) and Musca by N. B. Ngoc et al. (2024). Hence, it provides us a possible implication that this feature may be universal in dense and cold filaments. However, we need to explore more dense filamentary regions to strengthen the implication of the universality of this observed feature in dense filaments.

4.1.2. Increase in the Polarization Fraction with Dust Temperature

Another prediction of the RAT theory is that the polarization fraction should increase with increasing dust temperature (see, e.g., H. Lee et al. 2020; T. Hoang et al. 2021). In each of the regions of the filaments, both the polarization fraction P and the averaged grain alignment efficiency $P \times S$ increase with increasing dust temperature overall (see Figures 7 and 8(d)). This observed feature agrees well with the expectation of the RAT theory and provides us further evidence for the RAT alignment mechanism of grains.

4.1.3. Increase in a_{align} with I; Decrease in P and P \times S with a_{align}

Using the RAT-A theory, we calculate the minimum size for aligned grains by RATs using the local physical parameters and derive a map of alignment size (see Figure 9). Within the framework of the RAT-A theory, the size of aligned grains ranges from $a_{\rm align}$ to $a_{\rm max}$, and the polarization fraction is determined by this range of grain size. When $a_{\rm max}$ is fixed, an increase in the value of $a_{\rm align}$ can provide a narrower size distribution of aligned grains, which can result in the reduction of the polarization fraction P. Again, a decrease in $a_{\rm align}$ can result in a wider size distribution of aligned grains, which can increase P (see Figure 7 of L. N. Tram & T. Hoang 2022).



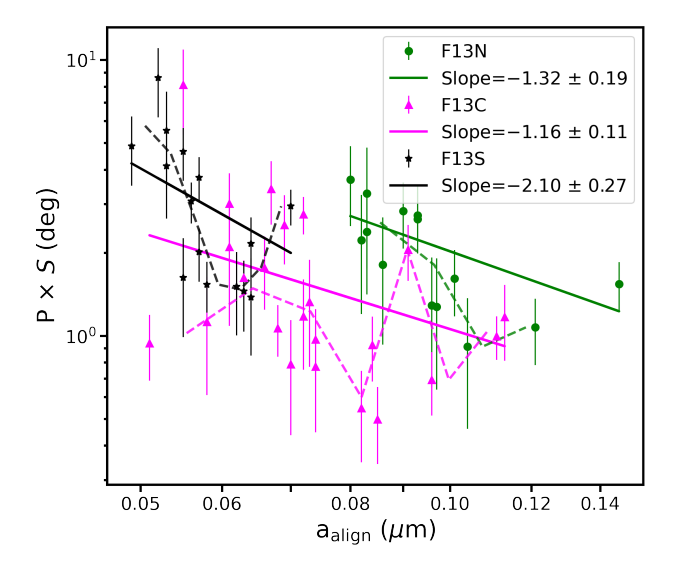


Figure 11. Variations of P with a_{align} (left) and $P \times S$ with a_{align} (right). The dashed lines are the weighted running means and the solid lines are the weighted best power-law fits.

Table 2 Slope Values of Weighted Best Power-law Fits for Different Analyses Using $P/\sigma_P>2$

Relation between	F13N	F13C	F13S
P versus I	-0.71 ± 0.09	-0.94 ± 0.04	-0.68 ± 0.05
P versus $N(H_2)$	-1.61 ± 0.23	-1.70 ± 0.07	-1.73 ± 0.14
$P \times S$ versus I	-0.73 ± 0.13	-0.70 ± 0.05	-0.86 ± 0.06
$P \times S$ versus $N(H_2)$	-1.85 ± 0.28	-1.06 ± 0.08	-2.53 ± 0.20
P versus $T_{\rm d}$	-1.37 ± 1.16	7.89 ± 0.37	5.57 ± 0.86
$P \times S$ versus $T_{\rm d}$	7.64 ± 1.23	2.27 ± 0.44	2.79 ± 1.49
a_{align} versus I	0.34 ± 0.09	0.29 ± 0.04	0.17 ± 0.03
P versus a_{align}	-0.42 ± 0.19	-1.95 ± 0.11	-1.46 ± 0.27
$P \times S$ versus a_{align}	-1.32 ± 0.19	-1.16 ± 0.11	-2.10 ± 0.27

Therefore, an anticorrelation is expected between a_{align} and P. Also, we expect a_{align} to increase with the total intensity I in starless clouds.

We find that the value $a_{\rm align}$ is well correlated with the intensity (see Figure 10), which means the alignment size increases in denser regions. The increasing of alignment size with intensity when no internal radiation source is present is an expectation of RAT-A theory. Also, there is anticorrelation in P with $a_{\rm align}$ and $P \times S$ with $a_{\rm align}$ (see Figure 11). These observed features support the RAT-A theory.

4.2. Role of Magnetic Relaxation in RAT Alignment: the M-RAT Mechanism

The study of the effect of enhanced magnetic relaxation, due to the expected superparamagnetic grains in the denser regions, on the RAT alignment of grains is important in the investigation of the exact alignment mechanism of grains. The observational potential evidence for the alignment of grains by the combined effects of both the suprathermal rotation by RATs and the enhanced magnetic relaxation strength or M-RAT mechanism was found in the previous studies in the G11.11-0.12 filament by N. B. Ngoc et al. (2023) and in the G34.43+0.24 filament by S. Pravash et al. (2025). In the F13 and F13S filaments, we find some pixels having high *P* values ranging from 6% to 15%. This observed high *P* values may not be produced by RAT only due to its dependence on factors

such as the angle between the directions of the radiation field and the magnetic field, grain shapes and compositions, etc. (T. Hoang & A. Lazarian 2016; J. Herranen et al. 2021). In our study, due to the limitation on the information of the estimated B_{POS} values to only some 24 pixels and the lack of information on the other pixels having polarization data, our estimation of the magnetic relaxation strength and the study of its effect on the RAT alignment are also limited to these 24 pixels only. There are other pixels showing high P values of around 15% but without B_{POS} information. However, some of these 24 pixels have high P values ranging from 5% to around 8%, mostly in the envelopes of the cores C2, C3, and C4 in the F13 filament and 6%-9.5% near cores C6 and C7 in the F13S filament. The pixels near the cores C2, C3, and C4 are also associated with typical gas volume densities of around $6 \times 10^3 \,\mathrm{cm}^{-3}$. These observed P values that reach around 8% in the envelopes of the C2, C3, and C4 cores can be considered as high values, and only RATs may not be able to produce these values. We also find some pixels having enhanced magnetic relaxation strength but showing lower P values in the F13C region, associated with higher a_{align} values.

We explore the importance of enhanced magnetic relaxation strength for the RAT alignment of grains and investigate whether the observed high P values in both the F13 and F13S filaments are purely due to the RAT alignment mechanism or M-RAT mechanism. When the magnetic relaxation occurs much faster than the gas collision damping, the magnetic relaxation strength is considered to be effective for the alignment of the grains. In the presence of both the suprathermal rotation of the grains by RATs and the enhanced magnetic relaxation strength, the RAT alignment efficiency of grains can be significantly increased (T. Hoang & A. Lazarian 2016; T. Hoang et al. 2022). Superparamagnetic grains can achieve perfect alignment by the M-RAT mechanism when $\delta_{mag,sp} >$ 10 (T. Hoang & A. Lazarian 2016). N. Chau Giang et al. (2024) found that observed high P values in the envelopes of protostellar cores could be produced by the thermal emission of the aligned superparamagnetic grains with $N_{\rm cl} \approx 10^2 - 10^3$, which can produce a high intrinsic polarization fraction. In our estimation of the magnetic relaxation strength in those 24 pixels in both the F13 and F13S filaments as shown

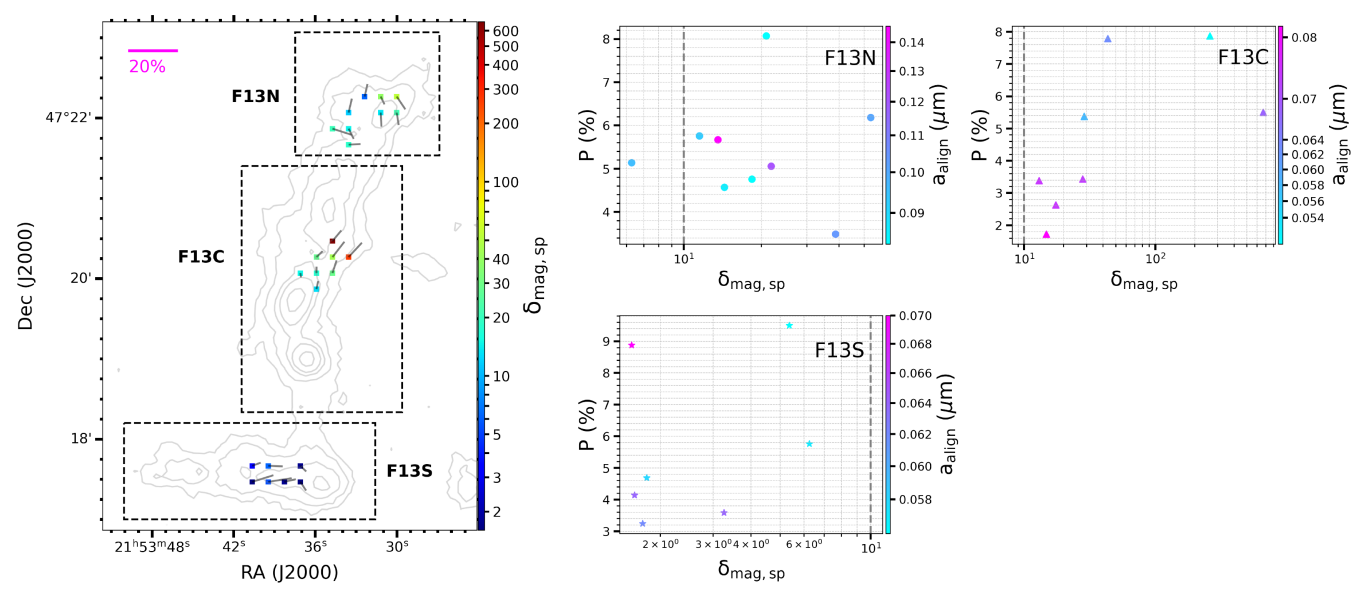


Figure 12. Map of magnetic relaxation strength $\delta_{\text{mag,sp}}$ with overlaid gray polarization vectors (left) and the relation between polarization fraction P and $\delta_{\text{mag,sp}}$ (right) in each region for only 24 pixels in total that have estimated values of magnetic field strength. The length of the gray vectors in the left panel is proportional to the polarization fraction P. A reference scale of P is also indicated. The vertical dashed gray lines denote $\delta_{\text{mag,sp}} = 10$. Most of the pixels in the F13N and F13C regions show $\delta_{\text{mag,sp}} > 10$. Some pixels have $\delta_{\text{mag,sp}} > 10$ with corresponding higher P values of around 5%–8% in the F13N and F13C regions. The pixels in the F13S region have $\delta_{\text{mag,sp}} \ll 10$.

in Figure 12, a small level of iron inclusions can produce $\delta_{\rm mag,sp}\gg 10$, especially in the F13N and F13C regions. However, we find $\delta_{\rm mag,sp}\ll 10$ in the F13S region.

In the F13N region, we find that some pixels that are associated with higher $a_{\rm align}$ values as well as higher $\delta_{\rm mag,sp}$ values have higher P values of around 6%. Here, only RATs may not be able to produce these high P values in these denser regions and the alignment of grains by the M-RAT mechanism can be significant. Again we see some pixels that have lower $a_{\rm align}$ values but $\delta_{\rm mag,sp} > 10$ have P values of around 4.6% that are lower but still high. However, we expect these pixels to have higher P values than the observed values. These smaller P values may be due to the local dominance of magnetic field tangling along the line of sight over the grain alignment in these particular pixels.

In the F13C region, we find that P increases with the simultaneous increase in $\delta_{\rm mag,sp}$ and the decrease in $a_{\rm align}$ (see Figure 12). This may imply the significant role of enhanced magnetic relaxation in the RAT alignment efficiency of grains. Some pixels that are associated with higher $a_{\rm align}$ values and found closer to the denser C2 core region show smaller P values even though $\delta_{\rm mag,sp} > 10$. This may be due to the saturation of the M-RAT alignment efficiency and the increase in the minimum alignment size of grains.

The enhanced magnetic relaxation combined with RATs can increase the alignment efficiency of grains and result in a higher polarization fraction. Given the limitation of the data and the study to only some pixels and also use of an estimated gas volume density by assuming cylindrical geometry of the filaments, a robust conclusion on the M-RAT mechanism cannot be drawn. However, our study in these limited pixels provides us potential hints for the possibility of a significant role of the M-RAT alignment mechanism in explaining the observed higher *P* values in some parts of the F13N and F13C regions.

For the F13S region, which is associated with weak magnetic fields, since $\delta_{\rm mag,sp} \ll 10$, the M-RAT mechanism

is found to be not efficient in this region and the observed higher P values are due to RATs only. The F13S filament is less dense than the F13 filament and is closer to the nearby B-type star BD+46. This region has higher dust temperature values than the F13 region and hence lower $a_{\rm align}$ values. Therefore, in this F13S region the RATs may be strong enough to produce efficient alignment of grains in the outer less dense regions due to its close proximity to the star BD+46, resulting in high P values.

Our study further supports the possibility of the M-RAT alignment mechanism (T. Hoang & A. Lazarian 2016) in the F13N and F13C regions of the F13 filament. All the discussions in Sections 4.1.1, 4.1.2, and 4.1.3 altogether provide us strong evidence for the possible explanation of the observed depolarization in the denser regions of the filaments by the decrease in the RAT alignment efficiency of grains in these regions. Also, from the discussion in Section 4.2 we get potential hints for the M-RAT alignment mechanism of grains in some of the regions of the F13 filament.

5. Conclusions

In this work, we investigate the dust grain alignment mechanisms in the F13 and F13S filamentary regions of the Cocoon Nebula (IC 5146) using observations of thermal dust polarization from the POL-2 instrument mounted on the James Clerk Maxwell Telescope at 850 μ m. We study the F13 region in the two subregions F13N and F13C that denote the North and Center regions of this filament. Our main results are summarized as follows.

1. We find that the polarization fraction P decreases with increasing total intensity I and gas column density $N(H_2)$, the so called polarization hole, in each of the F13N, F13C, and F13S regions. The polarization fraction P is found to increase with increasing dust temperatures $T_{\rm d}$ or equivalently increasing radiation field strength in each of the regions.

- 3. Further, to test whether the RAT-A mechanism can reproduce the observational results, we estimate the minimum alignment size of grains $a_{\rm align}$ for all the regions. We find that $a_{\rm align}$ increases with increasing I in each region, which is in agreement with the RAT-A theory. Again, from the analyses of the variations of P and $P \times S$ with $a_{\rm align}$, we find that the magnetic field tangling has no significant effect on the depolarization in each of the regions. The decrease in P and $P \times S$ with increasing $a_{\rm align}$ can be well explained by the RAT-A theory.
- 4. From all the analyses, we find strong evidence for the RAT-A mechanism that can explain that the observed depolarizations in the denser parts of the F13N, F13C, and F13S regions are due to the decrease in the RAT alignment efficiency of grains in these denser regions.
- 5. We also study the importance of magnetic relaxation for the RAT alignment of grains by estimating the magnetic relaxation strength. Our study finds that the observed high polarization fractions in some of the regions of the F13 filament may be potentially due to the combined effects of both the suprathermal rotation of grains by RATs and the enhanced magnetic relaxation strength, supporting the possibility of the magnetically enhanced RAT alignment mechanism of grains. This M-RAT mechanism is found to be not favorable in the F13S filament, which has weak magnetic fields, and the observed high *P* values in the outer regions of this filament can be due to efficient alignment of grains in the outer less dense regions by the strong RATs from the nearby B-type star BD+46.

Acknowledgments

This research has made use of observation data from the James Clerk Maxwell Telescope (JCMT) POL-2 instrument. JCMT is operated by the East Asian Observatory on behalf of the National Astronomical Observatory of Japan; Academia Sinica Institute of Astronomy and Astrophysics; the Korea Astronomy and Space Science Institute; the Operation, Maintenance and Upgrading Fund for Astronomical Telescopes and Facility Instruments, budgeted from the Ministry of Finance of China and administrated by the Chinese Academy of Sciences, and the National Key R & D Program of China. T.H. acknowledges the support from the main research project (No. 2025186902) from Korea Astronomy and Space Science Institute (KASI). P.N.D. and N.B.N. were funded by Vingroup Innovation Foundation (VINIF) under project code VINIF.2023.DA.057.

Facilities: JCMT, Herschel.

Software: Astropy (Astropy Collaboration et al. 2013, 2018); Scipy (P. Virtanen et al. 2020).

ORCID iDs

Saikhom Pravash https://orcid.org/0009-0002-6171-9740 Thiem Hoang https://orcid.org/0000-0003-2017-0982 Archana Soam https://orcid.org/0000-0002-6386-2906 Eun Jung Chung https://orcid.org/0000-0003-0014-1527 Diep Ngoc Pham https://orcid.org/0000-0002-2808-0888 Nguyen Bich Ngoc https://orcid.org/0000-0002-5913-5554 Le Ngoc Tram https://orcid.org/0000-0002-6488-8227

```
References
Alina, D., Montier, L., Ristorcelli, I., et al. 2016, A&A, 595, A57
Andersson, B. G., Lazarian, A., & Vaillancourt, J. E. 2015, ARA&A, 53, 501
André, P., Men'shchikov, A., Bontemps, S., et al. 2010, A&A, 518, L102
Arzoumanian, D., André, P., Didelon, P., et al. 2011, A&A, 529, L6
Astropy Collaboration, Price-Whelan, A. M., Sipőcz, B. M., et al. 2018, AJ,
   156, 123
Astropy Collaboration, Robitaille, T. P., Tollerud, E. J., et al. 2013, A&A,
  558, A33
Berry, D. S. 2015, A&C, 10, 22
Bethell, T. J., Chepurnov, A., Lazarian, A., & Kim, J. 2007, ApJ, 663, 1055
Chau Giang, N., Le Gouellec, V. J. M., Hoang, T., Maury, A. J., &
   Hennebelle, P. 2025, ApJ, 980, 33
Chung, E. J., Lee, C. W., Kim, S., et al. 2021, ApJ, 919, 3
Chung, E. J., Lee, C. W., Kim, S., et al. 2024, ApJ, 970, 122
Crutcher, R. M. 2012, ARA&A, 50, 29
Crutcher, R. M., Nutter, D. J., Ward-Thompson, D., & Kirk, J. M. 2004, ApJ,
   600, 279
Davis, L. J., & Greenstein, J. L. 1951, ApJ, 114, 206
Dolginov, A. Z., & Mitrofanov, I. G. 1976, Ap&SS, 43, 291
Draine, B. T. 2003, ARA&A, 41, 241
Draine, B. T. 2011, Physics of the Interstellar and Intergalactic Medium
   (Princeton, NJ: Princeton Univ. Press)
Draine, B. T., & Hensley, B. S. 2021, ApJ, 919, 65
Draine, B. T., & Weingartner, J. C. 1997, ApJ, 480, 633
Falceta-Gonçalves, D., Lazarian, A., & Kowal, G. 2008, ApJ, 679, 537
Friberg, P., Bastien, P., Berry, D., et al. 2016, Proc. SPIE, 9914, 991403
García-Rojas, J., Simón-Díaz, S., & Esteban, C. 2014, A&A, 571, A93
Hall, J. S. 1949, Sci, 109, 166
Herbig, G. H., & Reipurth, B. 2008, in Handbook of Star Forming Regions,
   Volume I, ed. B. Reipurth (San Francisco, CA: ASP), 108
Herranen, J., Lazarian, A., & Hoang, T. 2021, ApJ, 913, 63
Hildebrand, R. H. 1988, QJRAS, 29, 327
Hiltner, W. A. 1949, ApJ, 109, 471
Hoang, T., & Lazarian, A. 2008, MNRAS, 388, 117
Hoang, T., & Lazarian, A. 2014, MNRAS, 438, 680
Hoang, T., & Lazarian, A. 2016, ApJ, 831, 159
Hoang, T., Tram, L. N., Lee, H., Diep, P. N., & Ngoc, N. B. 2021, ApJ,
Hoang, T., Tram, L. N., Minh Phan, V. H., et al. 2022, AJ, 164, 248
Hoang, T., & Truong, B. 2024, ApJ, 965, 183
Jones, T. J. 1989, ApJ, 346, 728
Jones, T. J., Klebe, D., & Dickey, J. M. 1992, ApJ, 389, 602
Kaminsky, A., Bonne, L., Arzoumanian, D., & Coudé, S. 2023, ApJ, 948, 109
Lazarian, A. 2007, JQSRT, 106, 225
Lazarian, A., Andersson, B. G., & Hoang, T. 2015, in Polarimetry of Stars
   and Planetary Systems, ed. L. Kolokolova, J. Hough,
   A.-C. Levasseur-Regourd, 81 (Cambridge: Cambridge Univ. Press)
Lazarian, A., & Hoang, T. 2007, MNRAS, 378, 910
Lee, H., Hoang, T., Le, N., & Cho, J. 2020, ApJ, 896, 44
Myers, P. C. 2017, ApJ, 838, 10
Ngoc, N. B., Diep, P. N., Hoang, T., et al. 2023, ApJ, 953, 66
Ngoc, N. B., Hoang, T., Diep, P. N., & Tram, L. N. 2024, ApJ, 974, 118
Palmeirim, P., André, P., Kirk, J., et al. 2013, A&A, 550, A38
Panopoulou, G. V., Clark, S. E., Hacar, A., et al. 2022, A&A, 657, L13
Pattle, K., & Fissel, L. 2019, FrASS, 6, 15
Planck Collaboration, Aghanim, N., Akrami, Y., et al. 2020, A&A, 641, A12
Pravash, S., Soam, A., Diep, P. N., et al. 2025, ApJ, 981, 21
Purcell, E. M. 1979, ApJ, 231, 404
Sharpless, S. 1959, ApJS, 4, 257
Tram, L. N., & Hoang, T. 2022, FrASS, 9, 923927
Truong, B., & Hoang, T. 2025, ApJ, 981, 30
Virtanen, P., Gommers, R., Oliphant, T. E., et al. 2020, NatMe, 17, 261
Wang, J.-W., Lai, S.-P., Clemens, D. P., et al. 2020, ApJ, 888, 13
```